

Transient Superconductivity far above T_c in optically modulated $\text{YBa}_2\text{Cu}_3\text{O}_{6+x}$

S. Kaiser^{1,*}, D. Nicoletti^{1,*}, C.R. Hunt^{1,4}, W. Hu¹, I. Gierz¹, H.Y. Liu¹, M. Le Tacon²,
T. Loew², D. Haug², B. Keimer², and A. Cavalleri^{1,3}

¹ *Max Planck Institute for the Structure and Dynamics of Matter, Hamburg, Germany*

² *Max Planck Institute for Solid State Research, Stuttgart, Germany*

³ *Department of Physics, Oxford University, Clarendon Laboratory, Oxford, United Kingdom*

⁴ *Department of Physics and the Frederick Seitz Material Research Laboratory, University of
Illinois at Urbana-Champaign, Urbana, Illinois, USA*

** These authors contributed equally to this work.*

High intensity optical pulses at THz frequencies can be tuned to specific vibrational resonances and dynamically modulate the crystallographic structure of solids along a chosen normal-mode coordinate. This technique can be used to tip the balance between competing orders, or, as shown in the present paper, to create dynamically modulated states with effective properties different than at equilibrium. Femtosecond pulses at 20-THz frequency were used here to resonantly drive large-amplitude oscillations of the out-of-plane apical oxygen atoms in underdoped $\text{YBa}_2\text{Cu}_3\text{O}_{6+x}$. The modulated state is superconducting for base temperatures far above T_c , as evidenced by the appearance of a Josephson plasma edge in the c -axis reflectivity and a divergent imaginary optical conductivity σ_2 at low frequency. For $\text{YBa}_2\text{Cu}_3\text{O}_{6.5}$ transient superconductivity is observed up to room temperature, opening tantalizing prospects for optically-driven superconductivity in new regions of the cuprate phase diagram or in new materials.

Many experimental findings suggest that underdoped cuprates retain important properties of a superconductor above the equilibrium transition temperature $T_c^{\text{iii,iii}}$. The loss of long-range phase order is generally thought to be one of the key processes determining the transition to the normal state^{iv}. Hence, if the order-parameter phase could be stabilized either by design^v or by driving it with external fields^{vi}, superconductivity may become observable above T_c .

In this paper, we report on the use of THz-frequency optical fields to drive a specific dipole-carrying lattice distortion of $\text{YBa}_2\text{Cu}_2\text{O}_{6+x}$. In this way, the distance between the apical oxygen atoms and the Cu-O planes is periodically modulated (see Fig. 1). During modulation, a state with the transient low-frequency optical response typical of a superconductor is found for temperatures far above equilibrium T_c . The transient superconducting state is identified by the appearance of a sharp edge in the inter-layer optical reflectivity, observed at a characteristic frequency $\omega_J \sim 1.8$ THz. A similar feature is also measured in the optical response of the superconducting state at equilibrium and is typically attributed to coherent tunneling of Cooper pairs between the Cu-O planes. Such so-called Josephson plasma resonance is generally taken as a characteristic signature of superconductivity at equilibrium^{vii,viii}. As further evidence, our transient data also display a $1/\omega$ -like divergence in the frequency-dependent imaginary part of the optical conductivity $\sigma_2(\omega)$, as predicted by the London equations^{ix}.

Two underdoped compounds were studied, $\text{YBa}_2\text{Cu}_3\text{O}_{6.5}$ (YBCO 6.5) and $\text{YBa}_2\text{Cu}_3\text{O}_{6.6}$ (YBCO 6.6), with hole doping levels of 9% and 12% and superconducting transition temperatures $T_c = 50$ K and $T_c = 62$ K, respectively.

The samples were cut and polished along the *ac*-direction and were characterized by SQUID as well as by measuring their equilibrium THz optical response (see supplementary information S1).

Mid-infrared pump pulses of ~ 300 fs duration, polarized along the *c* direction and tuned to 20 ± 3 THz frequency ($\sim 15\text{-}\mu\text{m}$, 670 cm^{-1} , 83 meV , $\pm 15\%$), were made resonant with the infrared-active distortion shown in figure 1. These pulses were generated by difference-frequency mixing in an optical parametric amplifier. The pump pulses were focused to a maximum fluence of 4 mJ/cm^2 , corresponding to peak electric fields up to $\sim 3\text{ MV/cm}$.

The transient optical properties after mid-infrared excitation were probed in reflection by time-domain THz-spectroscopy^{x,xi}. Single-cycle THz probe pulses, with bandwidth covering the 0.5-2.5 THz spectral range, were generated by optical rectification of a near-infrared (800-nm wavelength) femtosecond pulse in a ZnTe crystal. These THz probe pulses were focused onto the YBCO crystals with polarization perpendicular to the superconducting planes (*c* axis), and were made to impinge onto the sample at variable time delays with respect to the mid-infrared pump pulses. The reflected THz transients were sampled electro-optically with a second near-infrared (800-nm wavelength) pulse in a second ZnTe crystal. At each time delay τ between mid-infrared pump and THz probe pulses, we obtained a trace $E_R(t, \tau)$, where t denotes the “internal delay” between THz transient and near-infrared sampling pulse. This technique yielded a transient measurement of the frequency-dependent complex optical properties between 0.5 and 2.5 THz for different time delays τ .

Figures 2A.1-3 summarize the “raw data” measured in YBCO 6.5 at 100 K. In Fig. 2A.1 the differential changes in the electric field transients $\Delta E_R(t, \tau) = E_R^{pumped}(t, \tau) - E_R^{unpumped}(t, \tau)$, normalized to the peak of the electric field reflected by the unperturbed sample E_R^{peak} , are shown for time delays $\tau = -5$ ps (black trace, no change) and $\tau = 0.8$ ps (red trace).

The corresponding changes in the frequency-dependent reflectivity $\frac{\Delta R}{R}(\omega, \tau)$ are shown in figure 2A.2. To obtain this quantity, the differential electric field transient $\Delta E_R(t, \tau)$ and the stationary reflected electric field $E_R(t)$ were independently Fourier transformed, yielding the complex valued frequency-dependent $\Delta \tilde{E}_R(\omega, \tau)$ and $\tilde{E}_R(\omega)$. From these and from the equilibrium $\tilde{r}(\omega)^{vii}$, we derived the complex reflection coefficient $\tilde{r}'(\omega, \tau)/\tilde{r}(\omega) = (\Delta \tilde{E}_R(\omega, \tau) + \tilde{E}_R(\omega))/\tilde{E}_R(\omega)$. The changes in the normal-incidence reflectivity were calculated as $\frac{\Delta R}{R}(\omega, \tau) = (|\tilde{r}'(\omega, \tau)|^2 - |\tilde{r}(\omega)|^2)/|\tilde{r}(\omega)|^2$.

The reflectivity change $\frac{\Delta R}{R}(\omega, 0.8 \text{ ps})$, displayed in figure 2A.2, already contains one of the key observations reported in this paper, a reflectivity edge near 1.8 THz, that is in the same frequency range as the Josephson plasma edge in the equilibrium superconducting state of YBCO 6.5^{vii,viii}.

In figure 2A.3 we show the time-delay dependence of this plasma edge, which disappears on a $\tau_0 \sim 1$ ps timescale, comparable with the decoherence time of the excited phonon, as determined by the inverse phonon linewidth in the optical conductivity^{vii,viii}. Thus, already from the relaxation time derived in the raw data, one can conclude that the light-induced effect is associated with the existence of a hot phonon, with no significant metastability after the vibration has relaxed.

Figures 2B.1-3 display the temperature dependence of the effect at $\tau = 0.8$ ps, which is the pump-probe time delay at which the optical response is maximum. As shown in figure 2B.2, the edge is clearly visible at 250 K. The size of the edge decreases with temperature up to nearly 300 K (figure 2B.3). We next turn to a quantitative evaluation of the data of figure 2. We first note that the size of the pump-induced reflectivity edge is significantly smaller than that observed in the reflectivity of superconductors at equilibrium. This is caused by the mismatch between the penetration depth of the 0.5-2.5 THz probe light, which is absorbed over several microns, and the 700-nm extinction depth for the resonant 20-THz pump pulse. Hence, the probe interrogates a volume that is between 10 and 20 times larger than the transformed region, with this mismatch varying as a function of frequency (see figure S2.1 in the supplementary information).

In figure 3 (panels 1 and 2) we show the recalculated frequency- and time-delay-dependent complex conductivity $\sigma_1(\omega, \tau) + i\sigma_2(\omega, \tau)$ of the photo-excited region alone, as derived from the measured reflectivity curves of figure 2 (see supplementary information S2). For all temperatures, no significant change was found in the real part of the conductivity σ_1 (panels 3.A.1-C.1), indicating that only minor rearrangements occur in the incoherent contribution to the spectral weight. Rather, the reflectivity response is dominated by changes in the imaginary part of the conductivity σ_2 .

The changes in σ_2 at 100 K are shown in figure 3A.2. The spectrum at negative time delay (black curve) reflects the out-of-plane properties at equilibrium: $\sigma_2(\omega, -5$ ps) is negative at all frequencies and extrapolates to zero for $\omega \rightarrow 0$. On the other hand, in the photo-stimulated state (red curve) $\sigma_2(\omega)$ is positive

and increases for decreasing ω . As shown in the figure (dashed curve) the increase can be fitted over the measured range with the same $1/\omega$ dependence predicted by the London equations, in direct correspondence to the zero-frequency delta function in the real part of the optical conductivity^{ix}. The assignment of transient superconductivity for photo-stimulated YBCO 6.5 at 100 K is further underscored by the comparison with the equilibrium data below T_c . The induced low-frequency transient conductivity σ_2 at 100 K (red curve) matches almost exactly that measured at equilibrium below T_c (dotted curve), as calculated from literature data^{vii}. This provides strong evidence for coherent interlayer transport far above T_c .

Finally, from the complex optical conductivity displayed in figures 3A.1 and 3A.2 we recalculate the reflectivity changes that one would observe if the entire probed volume was transformed. The recalculated reflectivity changes, displayed in figure 3A.3, show an edge that closely matches the Josephson plasma resonance observed in an equilibrium superconductor^{vii}.

The same qualitative features found at 100 K (Fig. 3A) are reproduced at 200 K and 280 K (Figs. 3B and 3C). Both the positive and diverging $\sigma_2(\omega)$ (panels 2) and the edge feature in the recalculated reflectivity changes (panels 3) indicate that the photo-induced superconducting state persists up to room temperature. However, the size of the effects is strongly reduced with increasing T .

In Figure 4, we report similar measurements for YBCO 6.6. A transient superconducting state is also observed far above T_c , although it vanishes well below room temperature.

In figure 5 we summarize all observations for these two doping levels. We display the transient superfluid density $D_{SF} = \lim_{\omega \rightarrow 0} \omega \sigma_2(\omega, 0.8 \text{ ps})$ in the photo-induced state as a function of base temperature for YBCO 6.5 (Fig. 5A) and YBCO 6.6 (Fig. 5B). In order to estimate an onset temperature of the transient superconducting state T' , we fit these temperature dependences to a gap equation^{xii,xiii}, which predicts a typical mean field square root dependence as $D^{SF} \propto \sqrt{1 - \frac{T}{T'}}$. This phenomenological fit yields $T'_{6.5} = 310 \pm 10 \text{ K}$ and $T'_{6.6} = 180 \pm 20 \text{ K}$. These results can then be pictorially summarized in the phase diagram of figure 5C, which highlights the region over which non-equilibrium superconductivity is achieved.

Essential information on the underlying mechanism for the formation of the transient superconducting state can be extracted from pump fluence and wavelength dependence of the induced superfluid density D_{SF} . This is displayed in figure 6 for the case of YBCO 6.5 at 100 K base temperature. We find that transient superconductivity is only observed above a threshold field of $\sim 700 \text{ kV/cm}$ (Fig. 6A). The key observation is that, over the field range explored in this work, the transient superfluid density increases linearly with the electric field. As derived in the supplementary information S3, the applied field strengths corresponds to a deformation of the apical oxygen position reaching $\sim 5\%$ of the unit cell, a number that is far larger than any static modulation method.

We note that in all other experiments that made use of optical excitation of lattice vibrations in complex solids, the effects observed scaled with the square of the field, as opposed to the linear dependence observed in this

experiment^{xiv}. A different mechanism than that observed in all previous lattice control experiments appears then to be at play here.

Secondly, as shown in figure 6B, the superfluid density of the light-induced state peaks when the pump wavelength is tuned to the phonon resonance, and rapidly decays for higher pump photon energies.

The effect found here cannot be explained by photo-induced redistribution of quasi-particles^{xv, xvi}, which was shown in the past to enhance superconductivity at microwave^{xvii, xviii, xix, xx, xxi} or optical^{xxii, xxiii} frequencies. Firstly, the lifetime of the state is not compatible with that of hot quasi-particles^{xxiv}. Secondly, quasi-particle excitations should lead to a response that scales linearly with intensity and thus quadratically with electric field, in contrast to the linear dependence displayed in figure 6A. Finally, the resonant response of figure 4B is incompatible with charge excitations, which should persist at photon energies higher than the phonon frequency.

One could argue that excitation of the lattice may be “melting” an ordered state that competes with superconductivity^{xxv}, as shown in the past for optically excited $\text{La}_{1.675}\text{Eu}_{0.2}\text{Sr}_{0.125}\text{CuO}_4$ ($\text{LESCO}_{1/8}$)^{xxvi}. However, as discussed above, unlike in the case of $\text{LESCO}_{1/8}$ and all previous experiments where vibrational excitation was used to melt competing orders^{xxvii, xxviii, xxix}, transient superconductivity survives here only for a time comparable to the decoherence time of the driven mode ($\tau_0 \sim 1$ ps), rather than relaxing into a long-lived state protected by a kinetic barrier.

We consider the physics of the system when the atoms are being periodically driven along the normal mode coordinate of figure 1. It is known that the electronic structure of cuprates correlates strongly with the position of the

apical oxygen atoms, as observed experimentally^{xxx} and extensively discussed theoretically^{xxxi,xxxii,xxxiii}. Important electronic properties in the Cu-O plane, including the super-exchange coupling, are expected to be modified when the apical oxygen is driven further away from the superconducting planes. In the periodically distorted state explored here, favorable parameters for coherent transport at higher temperatures may apply.

We also recall how dephasing in various physical systems can be inhibited by rapid modulation. This is well known for classical mechanics^{xxxiv,xxxv} or for Nuclear Magnetic Resonance^{xxxvi}, to mention only two of the most striking examples. As the 20-THz modulation used here occurs at frequencies high compared to plasma excitations between planes, one could envisage a dynamically stabilized stack of Josephson coupled planes. In the same spirit, the present observation was connected to the physics of Dicke superradiance in a recent paper, which suggested the formation of a coherent state by rapid modulation of a $k=0$ boson coupled to the electronic structure^{xxxvii}.

Our experiment may also provoke new thinking on the nature of the pseudogap state. We establish a temperature scale $T' \gg T_c$ below which the system acquires coherence upon modulation. One natural question pertains to the relation between T' and other temperature scales found when measuring physical properties of underdoped cuprates, such as the pseudogap temperature T^* or the temperature up to which phase fluctuations are observed, T_{Nernst} . There is an eye-catching graphic analogy between the onset temperatures of the non-equilibrium superconducting state shown in figure 5 and the pseudogap phase. The nature of the YBCO pseudogap state

should then be revisited from the point of view of its susceptibility to modulation.

In summary, we have used vibrational modulation in the mid infrared to induce transient superconducting transport in underdoped cuprates. Two different observations substantiate this conclusion. Firstly the out-of-plane imaginary part of the conductivity shows a London-type $1/\omega$ -divergence at low frequencies that matches that found at equilibrium below T_c . Secondly, the out-of-plane reflectivity shows the appearance of a Josephson plasma edge at approximately the same frequency as that observed below T_c . Strikingly, these properties can be induced far above T_c throughout the underdoped region of the phase diagram, reaching room temperature in $\text{YBa}_2\text{Cu}_3\text{O}_{6.5}$. The transient superconducting state is specific to the excitation of the apical oxygen mode, and it survives only as long as the mode is “hot”. It is concluded that the transient superconducting state is a property of the modulated solid.

Experiments that make use of fast femtosecond probes to interrogate lattice motions or charge and spin order after vibrational excitation, for example using scattering with a free electron laser^{xxxviii}, may provide important hints to understand the underlying physical pathway. Optimizing strength, bandwidth, and duration of the optical stimulation could stabilize coherent states on timescales long compared to the 1 ps observed in this work. Achieving this would open exciting prospects for optically-driven DC superconductors. More generally, a grand challenge for future research is to encapsulate our findings in a new class of theories that can describe the physics of coherently modulated unconventional superconductors.

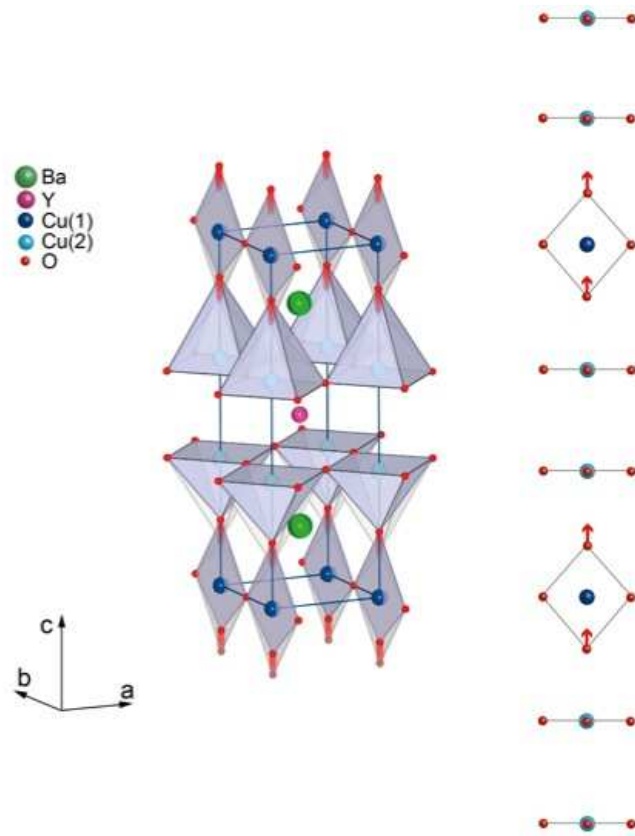


Figure 1. Structure of $\text{YBa}_2\text{Cu}_3\text{O}_{6.5}$ and lattice distortion for the 20 THz mode. Two conducting CuO_2 planes (Cu(2), and O in the ab -plane) are separated by Y atoms (pink) and form a bilayer unit. Ba atoms (green) and the CuO_4 ribbons (Cu(1), and O in the bc -plane) separate bilayer units^{xxxix}. The excitation of the infrared-active B_{1u} mode at 20-THz frequency modulates only the displacement of the apical oxygen atoms along the c direction^{viii,xl}.

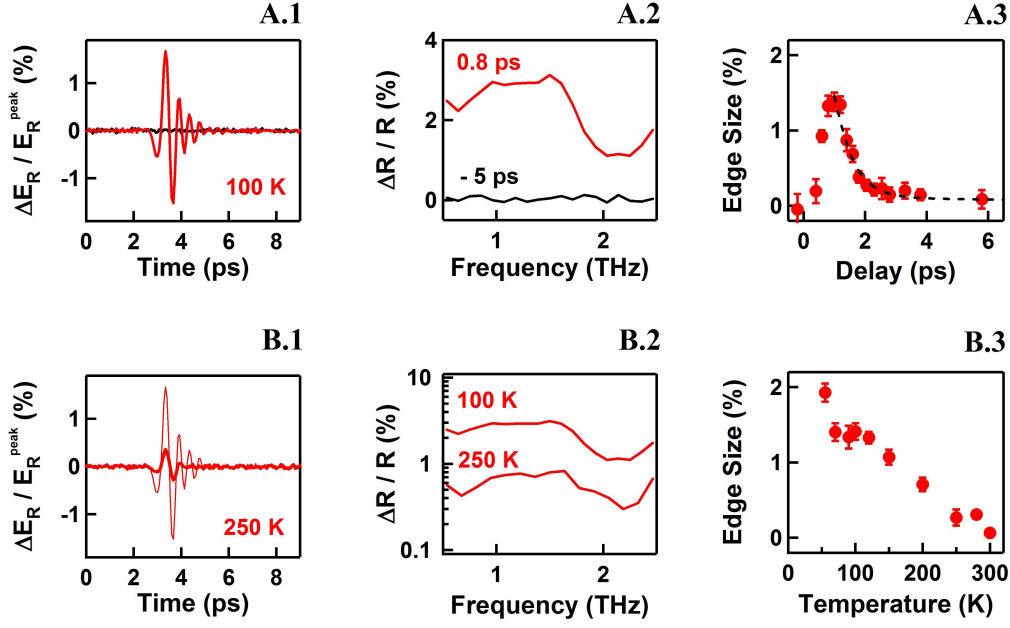


Figure 2. **(A.1)** Differential changes in the electric field transient ($\Delta E_R / E_R^{peak}$) in photo-stimulated YBCO 6.5 at 100 K, measured with THz pulses polarized along the c axis (perpendicular to the superconducting planes). The black curve (no change) corresponds to negative (-5 ps) time delay with respect to the 20-THz pump. The red curve corresponds to positive (+0.8 ps) time delay after the 20-THz pump. The measured differential $\Delta E_R(t, \tau)$ traces are normalized to the peak of the electric-field trace reflected by the unperturbed sample. **(A.2)** Corresponding frequency-dependent differential change in the reflectivity ($\Delta R / R$). A reflectivity edge at $\omega_f \sim 1.8$ THz is observed at 100 K, with a maximum size of ~ 1.5 % **(A.3)** Pump-probe time delay dependence of the edge size, defined as $\frac{\Delta R}{R}(\omega < \omega_f) - \frac{\Delta R}{R}(\omega > \omega_f)$. The decay of the edge (dashed line) takes place within ~ 1 ps. **(B.1)** Differential changes in the electric field transient ($\Delta E_R / E_R^{peak}$), measured for 0.8 ps time delay at 100 K (thin red curve, same as in figure A1) and at 250 K (thick red curve). **(B.2)** Frequency-dependent differential change in the reflectivity ($\Delta R / R$) at 100 K (same as red curve in figure A2) and 250 K. **(B.3)** Temperature dependence of the edge size for 0.8 ps time delay.

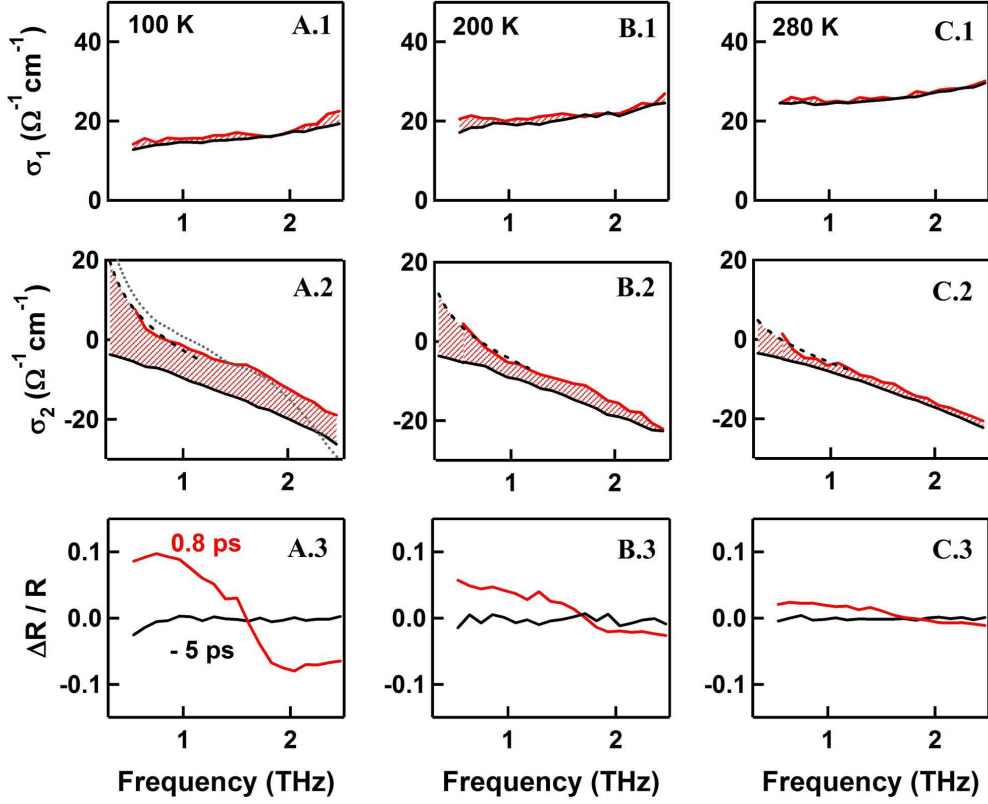


Figure 3. Recalculated transient optical properties of YBCO 6.5. **(A.1)** Real part of the optical conductivity $\sigma_1(\omega, \tau)$ at 100 K base temperature, as extracted from the measurements of figure 2A.1. Black curve: negative time delay before the 20-THz pump pulse. Red curve: positive time delay after the 20-THz pump pulse. **(A.2)** Imaginary part of the optical conductivity $\sigma_2(\omega, \tau)$ at 100 K. Dashed curve: fit to the conductivity assuming the functional form $\sigma_2(\omega) = \sigma_2^0(\omega) + D_{SF}/\omega$, where $\sigma_2^0(\omega)$ is the imaginary conductivity at equilibrium and D_{SF} is the transient superfluid density. Dotted curve: equilibrium imaginary conductivity of YBCO 6.5 measured below T_c^{vii} . **(A.3)** Reconstructed reflectivity for time delays of -5 ps (black curve) and 0.8 ps (red curve). The reconstruction assumes that the material is transformed over the whole penetration depth of the probe. **(B.1-3)** Conductivities and reconstructed reflectivities for 200 K base temperature, derived as in A.1-3. **(C.1-3)** Conductivities and reconstructed reflectivities for 280 K base temperature, derived as in A.1-3.

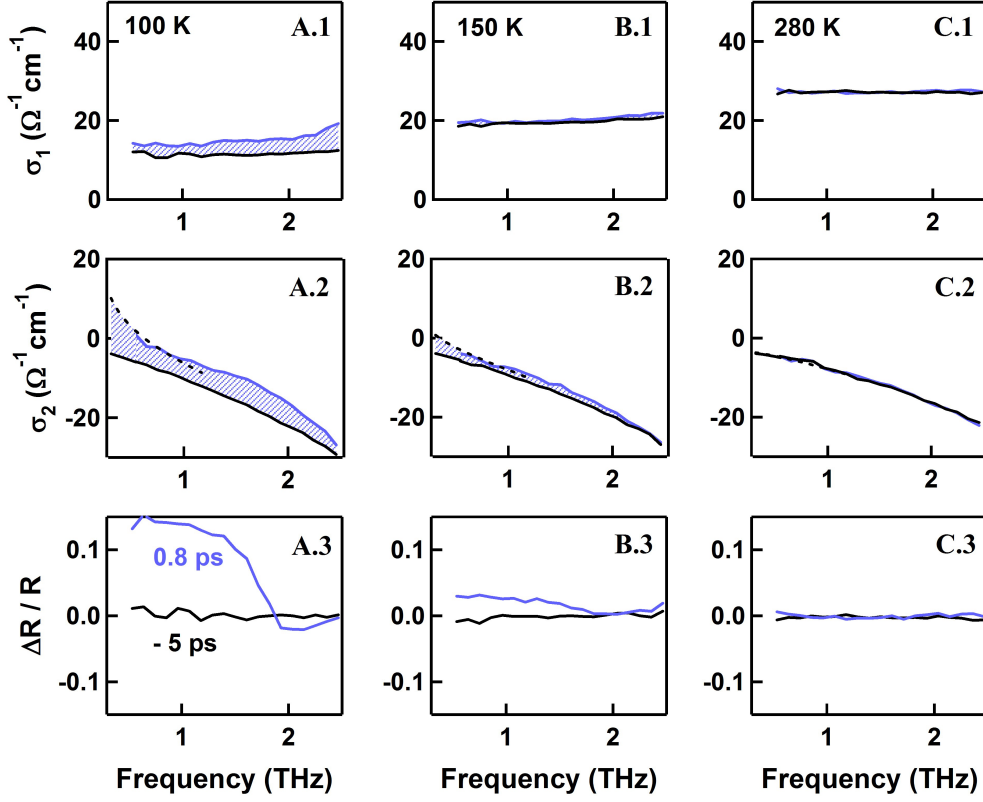


Figure 4. Recalculated transient optical properties of YBCO 6.6. **(A.1)** Real part of the optical conductivity $\sigma_1(\omega, \tau)$ at 100 K base temperature. Black curve: negative time delay before the 20-THz pump pulse. Blue curve: positive time delay after the 20-THz pump pulse. **(A.2)** Imaginary part of the optical conductivity $\sigma_2(\omega, \tau)$ at 100 K. Dashed curve: fit to the conductivity assuming the functional form $\sigma_2(\omega) = \sigma_2^0(\omega) + D_{SF}/\omega$, where $\sigma_2^0(\omega)$ is the imaginary conductivity at equilibrium and D_{SF} is the transient superfluid density. **(A.3)** Reconstructed reflectivity for time delays of -5 ps (black curve) and 0.8 ps (blue curve). The reconstruction assumes that the material is transformed over the whole penetration depth of the probe. **(B.1-3)** Conductivities and reconstructed reflectivities for 150 K base temperature, derived as in A.1-3. **(C.1-3)** Conductivities and reconstructed reflectivities for 280 K base temperature, derived as in A.1-3.

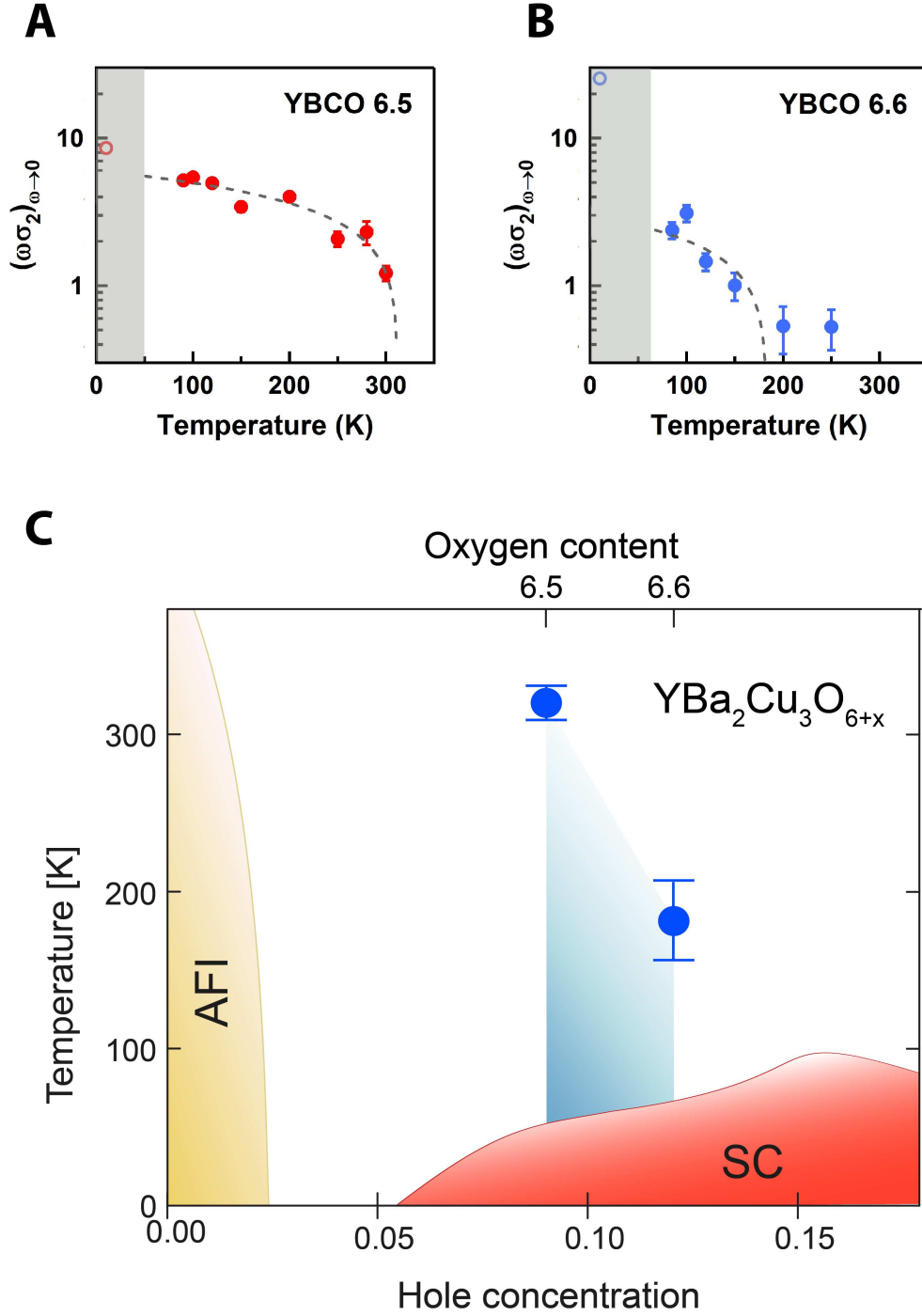


Figure 5. Transient superfluid density for **(A)** YBCO 6.5 and **(B)** YBCO 6.6 as a function of base temperature. The filled circles denote the transient superfluid density $D_{SF} = \lim_{\omega \rightarrow 0} \omega \sigma_2(\omega, \tau = 0.8 \text{ ps})$. The dashed line is a fit with a mean field gap equation, described in the text, used to define an onset temperature T' for non-equilibrium superconductivity. The region below the equilibrium T_c is colored in grey. Empty circles denote the equilibrium

superfluid density $D_{SF} = \lim_{\omega \rightarrow 0} \omega \sigma_2(\omega)$ below T_c . **(C)** Pictorial representation of a phase diagram for YBCO. The horizontal axes display the hole concentration (lower axis) and the oxygen content (upper axis). The vertical axis denotes the base temperature. The diagram highlights equilibrium antiferromagnetic (yellow) and equilibrium superconducting (red) phases. In blue, we show the region over which non-equilibrium superconductivity is found.

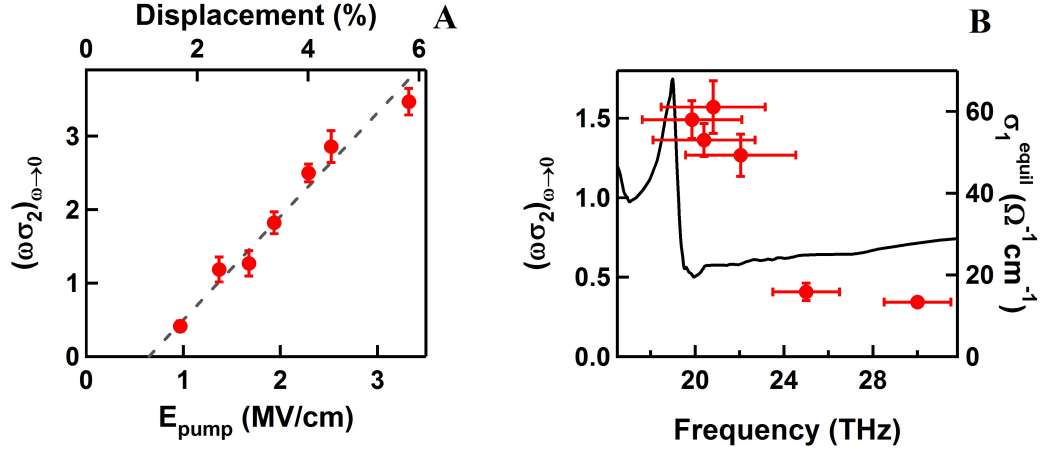


Figure 6. Transient superfluid density $D_{SF} = \lim_{\omega \rightarrow 0} \omega\sigma_2(\omega, 0.8 \text{ ps})$ of photo-excited YBCO 6.5 measured at 100 K base temperature. **(A)** D_{SF} plotted as a function of pump electric field. The horizontal axes denote the strength of the field (lower axis) and the apical oxygen displacement along the normal mode coordinate of figure 1 (upper axis), calculated using the procedure discussed in the supplementary information S3. **(B)**. D_{SF} plotted as a function of pump frequency (red dots, left axis) and compared to the equilibrium optical conductivity^{vii} in the same frequency region of the excited phonon mode (black curve, right axis). The horizontal error bars indicate the spectral width of the pump pulses.

SUPPLEMENTARY INFORMATION

S1 Sample Growth and Characterization

YBa₂Cu₃O_x crystals of typical dimensions 2 x 2 x 1 mm³ were grown in Y-stabilized zirconium crucibles¹. The hole doping of the Cu-O planes was adjusted by controlling the oxygen content of the CuO chain layer δ by annealing in flowing O₂ and subsequent rapid quenching.

The T_c values ($T_c = 50$ K for YBCO 6.5 and $T_c = 62$ K for YBCO 6.6) were determined by dc magnetization measurements, as shown in Figure S1A. The measured superconducting transition was found to be sharp in both samples ($\Delta T_c \sim 2 - 4$ K).

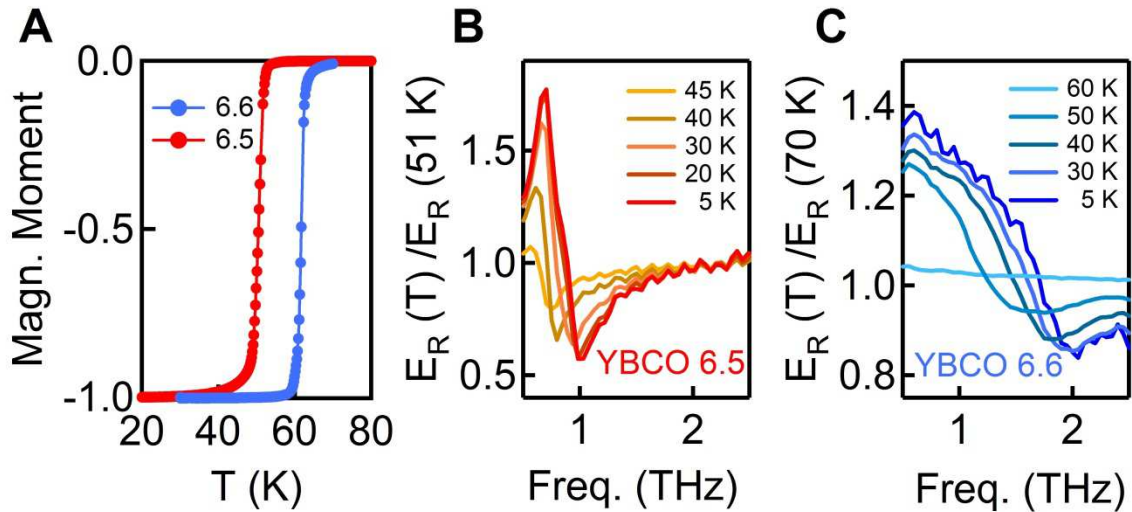


Figure S1 (A) SQUID characterization of the dc magnetization across the superconducting transition. (B) Josephson plasma resonance in the relative THz reflected field ratios for YBCO 6.5 and (C) YBCO 6.6 in the superconducting state.

¹ S. I. Schlachter, U. Tutsch, W. H. Fietz, et al., "Pressure effect and specific heat of RBa₂Cu₃O_x at distinct charge carrier concentrations: Possible influence of stripes", *Int. J. Mod. Phys. B* **14**, 3673 (2000).

The equilibrium optical properties of the two crystals were characterized by THz time-domain spectroscopy. Broadband THz pulses (0.5-2.5 THz) were focused onto the sample surface at 30° incidence, with polarization perpendicular to the Cu-O planes. The reflected electric field was measured by electro-optic sampling at different temperatures, below and above T_c .

Figure S1B and S1C show the absolute value of the frequency-dependent reflected electric field at a given temperature $|\tilde{E}_R(T)|$, normalized to the same quantity measured above T_c . In both materials, below T_c a strong edge appears at a frequency ω_J . This feature corresponds to the Josephson plasma resonance. The frequency ω_J increases with decreasing temperature, reaching $\omega_J(T \rightarrow 0) \sim 0.8$ THz for YBCO 6.5 and $\omega_J(T \rightarrow 0) \sim 1.4$ THz for YBCO 6.6.

S2 Derivation of the complex conductivity from differential reflectivity

At each mid-infrared pump / THz-probe time delay, τ , the pump-induced change in reflected electric field $\Delta E_R(t, \tau) = E_R^{pumped}(t, \tau) - E_R^{unpumped}(t, \tau)$ was measured (see traces in figure 2 in main text). The quantity $\Delta E_R(t, \tau)$ was acquired directly by filtering the electro-optic sampling signal with a lock-in amplifier, triggered by the signal from a mechanical chopper that modulated the mid-infrared pump. This measurement yielded “pump on” *minus* “pump off” reflected electric field. The reflected electric field from the unperturbed sample $E_R(t)$ was measured independently by placing the chopper on the THz beam.

The differential electric field $\Delta E_R(t, \tau)$ and the stationary reflected electric field $E_R(t)$ were independently Fourier transformed to obtain the complex

valued, frequency dependent $\Delta\tilde{E}_R(\omega)$ and $\tilde{E}_R(\omega)$. In those cases where the pump-induced changes to the reflected field were large enough, we also measured directly $\tilde{E}_R^{pumped}(\omega)$ and then calculated the quantity $\Delta\tilde{E}_R(\omega) = \tilde{E}_R^{pumped}(\omega) - \tilde{E}_R^{unpumped}(\omega)$, which agreed with the previous method. Finally, in order to rule out the possibility of phase drifts between $\Delta E_R(t, \tau)$ and $E_R(t)$, we also measured these two quantities at the same time, by simultaneously modulating mid-infrared pump and THz probe and filtering the signal with two lock-in amplifiers².

The complex reflection coefficient of the photo-excited sample, $\tilde{r}'(\omega, \tau)$, was determined from the normalized pump-induced changes to the electric field $\Delta\tilde{E}_R(\omega, \tau)/\tilde{E}_R(\omega)$ using the relation,

$$\frac{\Delta\tilde{E}_R(\omega, \tau)}{\tilde{E}_R(\omega)} = \frac{\tilde{r}'(\omega, \tau) - \tilde{r}(\omega)}{\tilde{r}(\omega)},$$

where the stationary reflection coefficient $\tilde{r}(\omega)$ was calculated from the equilibrium optical properties^{3,4}.

In practice, the “raw” reflectivity changes introduced above require reprocessing. Importantly, the measured changes are only few percent in size, due to a mismatch between the several- μm penetration depth of the 0.5-2.5 THz probe and that of the resonant 20-THz pump, which is tuned to the middle of the *reststrahlen* band for this particular phonon and is evanescent

² K. Iwaszczuk, D. G. Cooke, M. Fujiwara, H. Hashimoto, and P. U. Jepsen, “Simultaneous reference and differential waveform acquisition in time-resolved terahertz spectroscopy,” *Opt. Expr.* **17**, 21969 (2009).

³ C. C. Homes, T. Timusk, D. A. Bonn, et al., “Optical properties along the c-axis of $\text{YBa}_2\text{Cu}_3\text{O}_{6+x}$, for $x=0.5$ to 0.95 : evolution of the pseudogap”, *Physica C* **254**, 265 (1995).

⁴ C.C. Homes, T. Timusk, D. A. Bonn, R. Liang, and W.N. Hardy, “Optical phonons polarized along the *c*-axis of $\text{YBa}_2\text{Cu}_3\text{O}_{6+x}$, for $x = 0.5$ to 0.95 ,” *Can. J. Phys.* **73**, 663 (1995).

over a few hundred nm. At all frequencies, the probe interrogates a volume that is between 10 and 20 times larger than the transformed region beneath the surface, with this mismatch being a function of frequency (see figure S2.1). To extract the complex refractive index $\tilde{n}(\omega, \tau)$ of the photo-excited region, it was assumed that the change in $\tilde{n}(\omega, \tau)$ is maximum at the sample surface, decaying exponentially with distance, z , from the surface toward its unperturbed bulk value, $\tilde{n}_0(\omega)$, following Beer's law.

$$\tilde{n}(\omega, z) = \tilde{n}_0(\omega) + \Delta\tilde{n}(\omega)e^{-\alpha z},$$

where the linear extinction coefficient of the pump follows the inverse of the pump penetration depth, $\alpha = 1/d$.

The optical properties of the inhomogeneously excited medium were described by assuming a stack of layers of vanishing thickness δz , where $\tilde{n}(z) = \text{constant}$ for each layer⁵. For a single layer, j , the characteristic matrix of the sample may be written as

$$M_j = \begin{pmatrix} \cos(k_j \tilde{n}_j \delta z) & -\frac{i}{p_j} \sin(k_j \tilde{n}_j \delta z) \\ -ip_j \sin(k_j \tilde{n}_j \delta z) & \cos(k_j \tilde{n}_j \delta z) \end{pmatrix}.$$

Here the refractive index is $\tilde{n}_j = \tilde{n}(\omega, z = j\delta z)$, and we define $p_j = \tilde{n}_j \cos \theta_j$ for a TE mode and $p_j = \cos \theta_j / \tilde{n}_j$ for a TM mode. All measurements were taken in the TM configuration and with the THz probe oriented at $\theta_0 = 30^\circ$

⁵ M. Born and E. Wolf, "Principles of Optics," Pergamon Press.

from normal incidence. The quantity k_j is defined as $k_j = k_0 \cos \theta_j$, where the probe wave number in vacuum is $k_0 = \omega/c$.

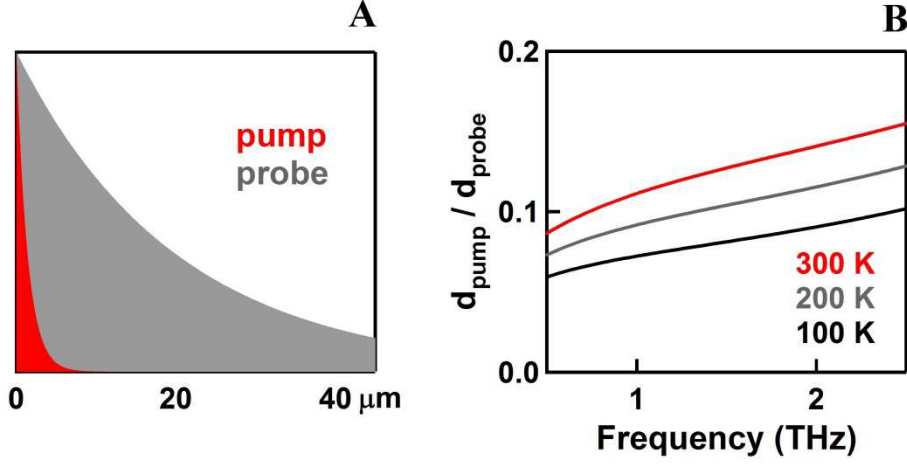


Figure S2.1. **A.** Schematic of the penetration depth mismatch between resonant vibrational excitation (20-THz frequency or 15- μm wavelength, red region) and the THz probe (0.5 – 2.5 THz, grey region). **B.** Ratio between penetration depths of pump (20 THz) and probe (0.5-2.5 THz).

The total characteristic matrix, M , is obtained as the product of the matrices for all layers, $M = \prod_{j=0}^N M_j$. The thickness of each layer is set such that $\delta z \ll d$, and the layers range from the sample surface to the probe penetration depth, $L = N\delta z$. From the elements of the total characteristic matrix, m_{ij} , we can extract the reflection coefficient,

$$\tilde{r}'(\omega) = \frac{(m_{11} + m_{12}p_L)p_0 - (m_{21} + m_{22}p_L)}{(m_{11} + m_{12}p_L)p_0 + (m_{21} + m_{22}p_L)}.$$

The quantity p_L is evaluated at the probe penetration depth and $p_0 = \cos \theta_0$ is calculated at the sample surface.

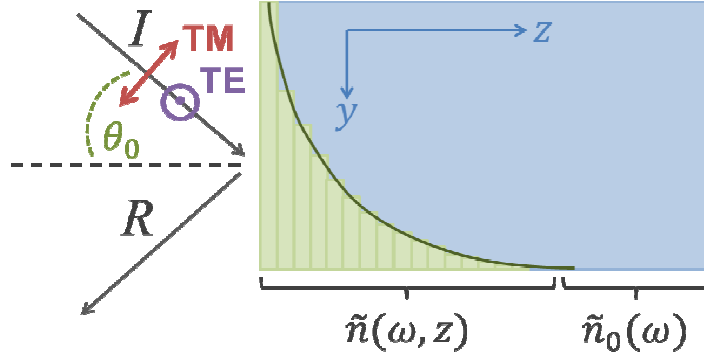


Figure S2.2. The refractive index of the excited crystal surface is approximated as a series of thin layers of constant $\tilde{n}(z)$. From layer to layer, the refractive index decays exponentially to the bulk value, $\tilde{n}_0(\omega)$. The incidence angle in the experiment is $\theta_0 = 30^\circ$.

This equation is solved numerically for the surface refractive index $\tilde{n}(\omega, \tau) = \tilde{n}_0(\omega) + \Delta\tilde{n}(\omega, \tau)$ using the Levenberg-Marquardt fitting algorithm in Matlab.

From the surface refractive index, we calculate the complex conductivity for a volume that is homogeneously transformed,

$$\tilde{\sigma}(\omega, \tau) = \frac{\omega}{4\pi i} [\tilde{n}(\omega, \tau)^2 - \varepsilon_\infty],$$

where $\varepsilon_\infty = 4.5$, a standard value for cuprates⁶.

In figures 3 and 4 in the main text the changes in the reflectivity, $\frac{\Delta R}{R}(\omega, \tau)$, are recalculated by assuming normal-incidence reflection,

$$R(\omega) = \left| \frac{1 - \tilde{n}(\omega)}{1 + \tilde{n}(\omega)} \right|^2.$$

⁶ D. van der Marel, H. J. A. Molegraaf, J. Zaanen, et al., "Quantum critical behaviour in a high- T_c superconductor," *Nature* **425**, 271 (2003).

As discussed in the main text, the photo-induced normal-incidence reflectivity displays a Josephson plasma edge at $\omega_J \sim 1.8$ THz. The calculated complex conductivity is also consistent with a photo-induced Josephson response, as $\sigma_1(\omega)$ remains relatively unchanged and $\sigma_2(\omega)$ turns positive and diverges at low frequencies below ω_J .

In the limit $d \ll L$ — which is relevant for the full spectral range, at all temperatures, considered in this paper — we find the multilayer model introduced above in full agreement with a single-layer approximation in which we consider only one excited layer, $N = 1$, with thickness $\delta z = d$ on an unperturbed bulk.

S3 Estimate of the field-induced lattice displacement

The amplitude of the field-induced atomic displacement due to mid-infrared photo-excitation can be estimated assuming an ionic bonding between the apical O^{2-} ion and the Cu(1) ion in the CuO chains.

The atomic polarizability can be derived as $\mathbf{P}(\omega_0) = \varepsilon_0 \chi(\omega_0) \mathbf{E}(\omega_0)$, where $\omega_0 = 20$ THz and $\|\mathbf{E}(\omega_0)\| \cong 3$ MV/cm. The susceptibility $\chi(\omega_0)$ is calculated from the c -axis equilibrium optical conductivity using $|\varepsilon_0 \chi(\omega_0)| = \left| \frac{\sigma(\omega_0)}{\omega_0} \right|$. As $|\sigma_1(\omega_0)| \cong |\sigma_2(\omega_0)| \cong 30 \Omega^{-1} \text{cm}^{-1}$ (from data in Refs. 3 and 4), one gets $|\varepsilon_0 \chi(\omega_0)| \cong 2 \cdot 10^{-12} \Omega^{-1} \text{cm}^{-1} \text{s}$ and $\|\mathbf{P}(\omega_0)\| \cong 6 \cdot 10^{-6} \text{C} \cdot \text{cm}^{-2}$.

The average size of the photo-induced electric dipole, i.e., the displacement of the oxygen ions, is then given by $d = \|\mathbf{P}(\omega_0)\|/nQ$, where n is the density of dipoles (2 per unit cell of volume 173 \AA^3) and $Q = 3e$. This yields $d \sim 10$ pm, which is approximately 5% of the equilibrium Cu-O distance.

REFERENCES (Main text)

- ⁱ Z. A. Xu, N. P. Ong, Y. Wang, T. Kakeshita, and S. Uchida, "Vortex-like excitations and the onset of superconducting phase fluctuation in underdoped $\text{La}_{2-x}\text{Sr}_x\text{CuO}_4$," *Nature* **406**, 486 (2000).
- ⁱⁱ D. N. Basov and T. Timusk, "Electrodynamics of high-T-c superconductors," *Rev. Mod. Phys.* **77**, 721 (2005).
- ⁱⁱⁱ A. Dubroka, M. Rössle, K. W. Kim, et al., "Evidence of a Precursor Superconducting Phase at Temperatures as High as 180 K in $\text{RBa}_2\text{Cu}_3\text{O}_{7-\delta}$ (R=Y,Gd,Eu) Superconducting Crystals from Infrared Spectroscopy," *Phys. Rev. Lett.* **106**, 047006 (2011).
- ^{iv} V. J. Emery and S. A. Kivelson, "Importance of Phase Fluctuations in Superconductors with Small Superfluid Density," *Nature* **374**, 434 (1995).
- ^v E. Berg, D. Orgad, and S. A. Kivelson, "Route to high temperature superconductivity in composite systems," *Phys. Rev. B* **78**, 094509 (2011).
- ^{vi} J. Hammer, M. Aprili, and I. Petkovic, "Microwave Cooling of Josephson Plasma Oscillations," *Phys. Rev. Lett.* **107**, 017001 (2011).
- ^{vii} C. C. Homes, T. Timusk, D. A. Bonn, et al., "Optical properties along the c-axis of $\text{YBa}_2\text{Cu}_3\text{O}_{6+x}$, for $x=0.5$ to 0.95 : evolution of the pseudogap", *Physica C* **254**, 265 (1995).
- ^{viii} C. C. Homes, T. Timusk, D. A. Bonn, R. Liang, and W. N. Hardy, "Optical phonons polarized along the c-axis of $\text{YBa}_2\text{Cu}_3\text{O}_{6+x}$, for $x = 0.5$ to 0.95 ," *Can. J. Phys.* **73**, 663 (1995).
- ^{ix} J. F. Annett, "Superconductivity, Superfluids and Condensates," Oxford Master Series in Condensed Matter Physics, Oxford, 2004.
- ^x R. D. Averitt, G. Rodriguez, A. I. Lobad, J. L. W. Siders, S. A. Trugman, and A. J. Taylor, "Nonequilibrium superconductivity and quasiparticle dynamics in $\text{YBa}_2\text{Cu}_3\text{O}_{7-\delta}$," *Phys. Rev. B* **63**, 140502 (2001).

-
- ^{xi} A. Pashkin, M. Porer, M. Beyer et al. "Femtosecond Response of Quasiparticles and Phonons in Superconducting $\text{YBa}_2\text{Cu}_3\text{O}_{7-\delta}$ Studied by Wideband Terahertz Spectroscopy," *Phys. Rev. Lett.* **105**, 067001 (2010).
- ^{xii} D. Einzel and I. Schürer, "Weak Coupling Theory of Clean (d+s)-Wave Superconductors," *Journal of Low Temperature Physics* **117**, 15 (1999).
- ^{xiii} M. Tinkham, "Introduction to Superconductivity," McGraw-Hill, New York, 1975.
- ^{xiv} M. Först, C. Manzoni, S. Kaiser, et al., "Nonlinear phononics as an ultrafast route to lattice control," *Nature Physics* **7**, 854 (2011).
- ^{xv} G. M. Eliashberg, "Film Superconductivity Stimulated by a High-frequency Field," *JETP Letters* **11**, 114 (1970); B. I. Ivlev and G. M. Eliashberg, "Influence of Nonequilibrium Excitations on the Properties of Superconducting Films in a High-frequency Field," *JETP Letters* **13**, 333 (1971).
- ^{xvi} C. S. Owen and D. J. Scalapino, "Superconducting State under the Influence of External Dynamic Pair Breaking," *Phys. Rev. Lett.* **28**, 1559 (1972).
- ^{xvii} P. W. Anderson and A. H. Dayem, "Radio-Frequency Effects in Superconducting Thin Film Bridges," *Phys. Rev. Lett.* **13**, 195 (1964).
- ^{xviii} A. F. G. Wyatt, V. M. Dmitriev, W. S. Moore, and F. W. Sheard., "Microwave-Enhanced Critical Supercurrents in Constricted Tin Films," *Phys. Rev. Lett.* **16**, 1166 (1966).
- ^{xix} A. H. Dayem and J. J. Wiegand, "Behavior of Thin-Film Superconducting Bridges in a Microwave Field," *Phys. Rev.* **155**, 419 (1967);
- ^{xx} R. Escudero and H. J. T. Smith, "Energy-gap enhancement in superconducting tin by microwaves," *Phys. Rev. B* **31**, 2725 (1985)
- ^{xxi} S. I. Vedenev, D. K. Maude, and J. M. Byrne, "Microwave enhancement of superconductivity in $\text{Bi}_2\text{Sr}_2\text{CaCu}_2\text{O}_{8+\delta}$ break junctions," *Phys. Rev. B* **78**, 052509 (2008)

-
- ^{xxii} G. Yu, C. H. Lee, A. J. Heeger, N. Herron, and E. M. McCarron, "Transient photoinduced conductivity in single crystals of $\text{YBa}_2\text{Cu}_3\text{O}_{6.3}$: "Photodoping" to the metallic state," *Phys. Rev. Lett.* **67**, 2581 (1991).
- ^{xxiii} G. Nieva, E. Osquiguil, J. Guimpel et al. "Photo-induced Enhancement of Superconductivity," *Appl. Phys. Lett.* **60**, 2159 (1992).
- ^{xxiv} G. P. Segre, N. Gedik, J. Orenstein, D. A. Bonn, R. Liang, and W. N. Hardy, "Photoinduced Changes in Reflectivity in Single Crystals of $\text{YBa}_2\text{Cu}_3\text{O}_{6.5}$ (ortho II)" *Phys. Rev. Lett.* **88**, 137001 (2002).
- ^{xxv} G. Ghiringhelli, M. Le Tacon, M. Minola, et al., "Long-Range Incommensurate Charge Fluctuations in $(\text{Y,Nd})\text{Ba}_2\text{Cu}_3\text{O}_{6+x}$," *Science* **337**, 821 (2012).
- ^{xxvi} D. Fausti, R. I. Tobey, N. Dean. et al. "Light induced superconductivity in a striped ordered cuprate," *Science* **331**, 189 (2011).
- ^{xxvii} M. Rini, R. I. Tobey, N. Dean, et al. "Control of the electronic phase of a manganite by mode-selective vibrational excitation," *Nature* **449**, 72 (2007).
- ^{xxviii} R. I. Tobey, D. Prabhakaran, A. T. Boothroyd, and A. Cavalleri, "Ultrafast Electronic Phase Transition in $\text{La}_{1/2}\text{Sr}_{3/2}\text{MnO}_4$ by Coherent Vibrational Excitation: Evidence for Nonthermal Melting of Orbital Order," *Phys. Rev. Lett.* **101**, 197404 (2008).
- ^{xxix} A. D. Caviglia, R. Scherwitzl, P. Popovich, et al., "Ultrafast Strain Engineering in Complex Oxide Heterostructures," *Phys. Rev. Lett.* **108**, 136801 (2012).
- ^{xxx} J. A. Slezak, J. Lee, M. Wang, et al. "Imaging the impact on cuprate superconductivity of varying the interatomic distances within individual crystal unit cells," *Proc. Nat'l Acad. Scie. USA* **105**, 3203 (2008).
- ^{xxxi} E. Pavarini, I. Dasgupta, T. Saha-Dasgupta, et al., "Band-Structure Trend in Hole-Doped Cuprates and Correlation with $T_{c,\text{max}}$," *Phys. Rev. Lett.* **87**, 047003 (2001).

^{xxxiii} C. Weber, K. Haule, and G. Kotliar, “Apical oxygens and correlation strength in electron- and hole-doped copper oxides,” *Phys. Rev. B* **82**, 125107 (2010).

^{xxxiii} M. Mori, G. Khaliullin, T. Tohyama, and S. Maekawa “Origin of the spatial variation of the pairing gap in Bi-based High Temperature Cuprate Superconductors,” *Phys. Rev. Lett.* **101**, 247003 (2008).

^{xxxiv} P. L. Kapitza, “Dynamic stability of a pendulum with an oscillating point of suspension,” *Zh. Eksp. Teor. Fiz.* **21**, 588 (1951).

^{xxxv} L. D. Landau and E. M. Lifschitz, *Mechanics* (Pergamon, Oxford 1976).

^{xxxvi} A. W. Overhauser, “Polarization of Nuclei in Metals,” *Phys. Rev.* **92**, 411 (1953).

^{xxxvii} G. Baskaran, “Superradiant Superconductivity,” *arXiv:1211.4567* (2012).

^{xxxviii} M. Först, R.I. Tobey, S. Wall, et al., “Driving magnetic order in a manganite by ultrafast lattice excitation,” *Phys. Rev. B* **84**, 241104(R) (2011)

^{xxxix} G. Calestani and C. Rizzoli, “Crystal structure of the YBa₂Cu₃O₇ superconductor by single-crystal X-ray diffraction,” *Nature* **328**, 606 (1987).

^{xl} G. Burns, F. H. Dacol, P. P. Freitas, et al., “Phonons in YBa₂Cu₃O_{7-δ}-type materials,” *Phys. Rev. B* **37**, 5171 (1988).